catalysts

MDPI

Article

Cyanogel-Based Preparation of Amorphous NiFe Nanoaggregates with Enhanced Activity and Stability for OER

Shun Li [1,†], Jinxin Wan [1,†], Zhenyuan Liu [1,*], Mengdie Zhuang [1], Pengyuan Ren [2,*], Weilong Shi [1], Xiaojun Zeng [3] and Jun Yang [1,*]

[1] School of Materials Science and Engineering, Jiangsu University of Science and Technology, Zhenjiang 212100, China
[2] School of Civil Engineering and Architecture, Jiangsu University of Science and Technology, Zhenjiang 212100, China
[3] School of Materials Science and Engineering, Jingdezhen Ceramic University, Jingdezhen 333403, China
* Correspondence: zhenyuanliu@just.edu.cn (Z.L.); renpengyuan@just.edu.cn (P.R.); iamjyang@just.edu.cn (J.Y.)
† These authors contributed equally to this paper.

Abstract: The development of cost-efficient electrocatalysts for oxygen evolution reaction (OER) with high efficiency is crucial to widespread applications of water splitting for hydrogen production. In this work, porous three-dimensional (3D) amorphous NiFe nanoaggregates composed of interconnected nanograins were synthesized by a cyanogel-based wet chemical reduction method using the $NiCl_2/Na_4Fe(CN)_6$ cyanogel as the precursor and $NaBH_4$ as the reducing agent. The influence of the incorporated Fe amount was carefully studied by slightly changing the feeding molar ratios of the Ni/Fe atoms in the precursors. The intrinsic 3D backbone structure of the cyanogel resulted in crystal nuclei tending to generate along with the backbones, which is key to the formation of NiFe nanoaggregates with a porous 3D interconnected structure. The synthesized NiFe nanoaggregates with a 3D interconnected structure and high porosity, as well as the incorporation of Fe, are in favor of high surface area, more active sites, and abundant oxygen vacancies, leading to superior activity and stability of OER in alkaline electrolytes with a low overpotential of 0.35 V at 10 mA cm^{-2}, a high current density of 24.8 mA cm^{-2} at 1.65 V, a small Tafel slope of 76.9 mV dec^{-1}, and attractive durability in 1 M KOH solution.

Keywords: amorphous NiFe; cyanogel; oxygen vacancies; oxygen evolution reaction

Citation: Li, S.; Wan, J.; Liu, Z.; Zhuang, M.; Ren, P.; Shi, W.; Zeng, X.; Yang, J. Cyanogel-Based Preparation of Amorphous NiFe Nanoaggregates with Enhanced Activity and Stability for OER. *Catalysts* **2023**, *13*, 1261. https://doi.org/10.3390/catal13091261

Academic Editor: Barbara Mecheri

Received: 1 August 2023
Revised: 23 August 2023
Accepted: 29 August 2023
Published: 31 August 2023

1. Introduction

With the increasing demand on traditional fossil fuels and corresponding environmental pollution, it is important to develop clean, sustainable, and carbon-free energy such as hydrogen energy. Oxygen evolution reaction (OER) has been identified as a crucial half reaction of electrochemical water splitting for hydrogen production due to its complicated four-electron transfer process to oxidize two water molecules, including the breakdown of O−H bonds and generation of O=O bonds [1–5]. Moreover, a high overpotential is usually required to carry out this reaction. On account of the intrinsically sluggish reaction kinetics and high overpotential of OER, it cannot be widely applied for commercialization. Therefore, the development of highly efficient and stable electrochemical catalysts for OER is imperative to improve the energy conversion efficiency and promote industrialization.

The ideal OER catalyst must have high electrocatalytic activity and durability, high porosity and accessibility for liquid and gas transport, and be synthesized by green and cost-effective approaches. Up to now, noble metal-based electrocatalysts (such as IrO_2 and RuO_2) have been recognized as highly efficient electrocatalysts for OER, but their high cost, scarcity, and poor stability hamper their widespread application in energy devices [6–8]. Great efforts are currently focused on finding alternative inexpensive and earth-abundant non-noble catalysts for OER, such as transition metal alloys [9,10], oxides [11,12], hydroxides [13,14],

phosphides [15,16], and nitrides [17,18]. In recent studies, 3*d* transition metal nickel-based materials have been identified as one of the most promising OER catalysts [19–22]. For example, Lou's group synthesized NiCo nanocatalysts atomically dispersed on nitrogen-doped carbon hollow prisms by a multi-step templating method, and the smallest Tafel slope of 49 mV dec^{-1} and an overpotential of 252 mV at a current density of 10 mA cm^{-2} was exhibited for OER [19]. Zhang's group introduced cation vacancies in the basal plane of NiFe LDH to enhance OER performance, with only 2.22% of activity degradation after 1000 cyclic voltammetry (CV) cycles [20]. Ji's group developed carbon-wrapped bimetallic NiCo nanospheres with a simple annealing process, which only required an overpotential of 330 mV for OER to reach a catalytic current density of 10 mA cm^{-2} [10]. It is worth noting that doping a foreign 3*d* transition metal atom (such as Fe) into the Ni lattice can adjust the electronic structures of Ni, thus improving the OER performance. NiFe LDHs-V_{Fe} and NiFe LDHs-V_{Ni} electrocatalysts only need an overpotential of 245 and 229 mV, respectively, to obtain a geometric catalytic density of 10 mA cm^{-2} for OER, which is due to the introduction of rich Fe or Ni vacancies in NiFe LDHs nanosheets being able to efficiently modify the surface electronic structure [21]. Fe-doped NiS_2 microcrystals with exposed chemically stable {001} facets synthesized by the hydrothermal method exhibited superior OER performance, with a small overpotential of 277 mV at a current density of 10 mA cm^{-2} [22]. Fe-doped β-$Ni(OH)_2$ interconnected hierarchical nanosheets on nickel foam via a conventional hydrothermal reaction showed significant improvements in electrochemical performance of OER (overpotential: 189 mV; Tafel slope: 85 mV dec^{-1}) [13].

On the other hand, three-dimensional (3D) nanostructures with abundant pores could provide high surface area and excellent molecular accessibility, promote mass diffusion, and increase the utilization efficiency of metal atoms [23–25]. Furthermore, 3D structures could prevent nanoparticles from agglomerating and deactivating during the electrocatalysis process because of their self-supportability, thereby exhibiting excellent durability [26–28]. Owing to these structural advantages, many efforts have been devoted to synthesizing porous 3D transition metal-based nanocatalysts. For instance, Zeng's group synthesized a 3D CoFePi network with a bitemplate coprecipitation approach at room temperature with superior OER electrocatalytic activity, which yielded an overpotential of 315 mV at 10 mA cm^{-2} and a Tafel slope of 33 mV dec^{-1} [26]. Lee's group reported a unique 3D hierarchical network derived from 2D Fe-doped NiSe nanosheets and carbon nanotubes, which exhibited enhanced OER performance with an overpotential of only 282.7 mV at 10 mA cm^{-2} for overall water splitting [27]. However, the present synthetic methods for transition metal-based nanocatalysts usually suffer from tedious and harsh etching procedures, such as the hard template-engaged method [19,29,30], electrodeposition [31,32], and so forth. Therefore, the preparation of transition metal-based 3D nanostructures with high porosity through a simple and economical approach is highly desirable.

Herein, we develop a porous 3D NiFe nanoaggregate with amorphous structure through a surfactant-free cyanogel-$NaBH_4$ chemical reduction approach at room temperature as an efficient OER electrocatalyst (Equation S2). Cyanogel is a special class of 3D double-metal coordination polymer generated through a reaction between tetrachlorometalates and transition metal cyanometalates in aqueous solution (Equation S1) [33–35]. The formation of cyanide-bridged structure was due to the substitution of two chloride ligands by the nitrogen end of the cyanide ligands on an M metal center [23,36]. Because the cyanide bridges are central to these gels, distinguishing them from classic metal–oxo gels, these gels are referred as cyanogels. Resulting from the homogeneous distribution of different metal ions on 3D backbones, cyanogel could be used as a precursor to synthesize nanoalloys with 3D nanostructures. Therefore, the Ni-Fe cyanogel is initially prepared with the reaction of $NiCl_2$ and $Na_4Fe(CN)_6$ solutions, which can be reduced to form 3D NiFe nanoaggregates with abundant pores after adding fresh $NaBH_4$ solution. Benefiting from the advantages of composition and the porous 3D interconnected structure, the as-synthesized NiFe nanoaggregates exhibit superior activity and stability for OER compared with other referred samples and commercial RuO_2 in alkaline electrolytes.

2. Results and Discussion

Figure 1 schematically shows the overall synthetic process of forming NiFe nanoaggregates, including the gelation of Ni-Fe cyanogels and chemical reduction using freshly prepared $NaBH_4$ solution. The Ni-Fe cyanogels were firstly formed by simply mixing $NiCl_2$ and $Na_4Fe(CN)_6$ solutions. The successful gelation of Ni-Fe cyanogels was proven by Fourier transform infrared (FT-IR) tests. The peak located at 2164 cm^{-1} is the characteristic stretching peak of C≡N (Figure S1), which showed a positive shift compared to that of $Na_4Fe(CN)_6$ (2144 cm^{-1}), indicating the successful formation of Ni-Fe cyanogels [37,38]. In the low-wavenumber region, there was a major peak located at 588 cm^{-1} assigned to an Fe-CN-Ni bending mode. During the gelation process, the nitrogen end of cyanide ligand in $Na_4Fe(CN)_6$ replaced the transchloride ligand in $NiCl_2$. After the addition of fresh $NaBH_4$ solution to the Ni-Fe cyanogels, the CN-bridged Ni^{2+} and Fe^{2+} ions were simultaneously reduced to NiFe nanoaggregates (Equation S2). So as to study the effect of Fe contents, three kinds of Ni-Fe cyanogels with different feeding molar ratios of $NiCl_2/Na_4Fe(CN)_6$ (1:1, 2:1, and 3:1) were synthesized, followed by $NaBH_4$ reduction under the same experimental conditions. The obtained samples were named NiFe-11, NiFe-21, and NiFe-31, respectively.

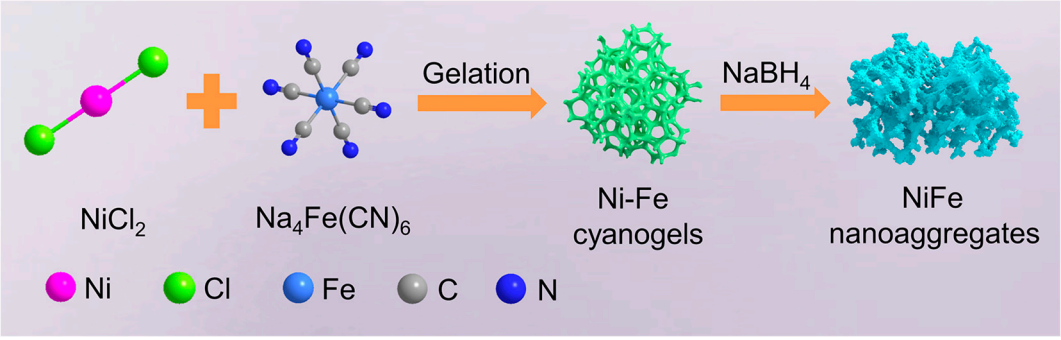

Figure 1. Schematic illustration of the formation of NiFe nanoaggregates through a cyanogel-based strategy.

The crystal structure of the product was identified by X-ray diffraction (XRD) pattern. As shown in Figure 2a, a broadened diffraction peak located at about 45.3° suggests that the obtained NiFe nanoparticles had an amorphous nature. Studies have shown that, compared to high-crystalline materials, nanostructures with an amorphous nature have abundant unsaturated chemical bonds and defects, which can provide more active sites for target molecules and facilitate the adsorption of active intermediates at the electrode/electrolyte interface during catalytic reactions [39]. Thus, the resulting amorphous NiFe-21 nanostructure showed improved OER performance. The morphological features of the amorphous NiFe-21 were investigated by scanning electron microscopy (SEM) and transmission electron microscopy (TEM). Figure 2b displays the typical SEM image of the NiFe-21 nanostructures. Obviously, the NiFe-21 showed a porous 3D continuous aggregate structure made up of interconnected nanoparticles. In agreement with the SEM results, the TEM image further validated the continuous aggregate structure of the NiFe-21 nanomaterials (Figure 2c), and no solitary particles appeared, indicating structural integrity. The high-resolution TEM (HRTEM) image (Figure 2d) shows that the NiFe-21 nanostructures had abundant pores and consisted of plentiful interconnected small nanograins with a diameter around 8 nm. The formation of an interconnected 3D nanostructure was due to the characteristic 3D backbone structure of cyanogels, which hampered the migration of reduced metal nuclei and resulted in the growth of metals along the 3D skeletons. Such an interconnected 3D nanostructure effectively prevented the collapse of the structures from dissolution and agglomeration. In addition, the porous nanostructure and interconnected small nanograins led to the NiFe-21 nanoaggregates affording more active sites and a larger active surface area, as well as facilitating the gas diffusion and mass transport of target molecules, thus enhancing the electrochemical properties. As for the samples of NiFe-11 and NiFe-31, the SEM images are shown in Figure S2. It can be seen that the NiFe-11 still

retained the porous 3D interconnected nanostructure (Figure S2a,b), but the collapse of the 3D interconnected structure occurred on NiFe-31 (Figure S2c,d). This may have resulted from the decrease in Fe, leading to the excessive Ni atoms not being able to combine with cyano groups and being reduced alone. The elemental mappings were used to describe the distributions of the compositions in the catalysts. Figure 2e displays the high-angle annular dark field–scanning transmission electron microscopy (HAADF-STEM) and elemental mapping images of the amorphous NiFe-21 nanoaggregates, which manifests that the Ni and Fe were homogeneously distributed throughout the nanostructures. This conclusion was further proven by the EDX line-scanning profile, where Ni and Fe signals appeared during the line-scanning process (Figure S3). What is more, the molar ratio of Ni/Fe in NiFe-21 nanoaggregates was 83.7:16.3, calculated from the EDX spectrum (Figure S4), which is a little bigger than that of the feeding molar ratio (2:1). This may be because Fe was much easier to oxidize than Ni during the reduction process, and the oxidized Fe tended to enter the solution rather than remain on the metallic skeleton, resulting in the loss of Fe in the synthesis.

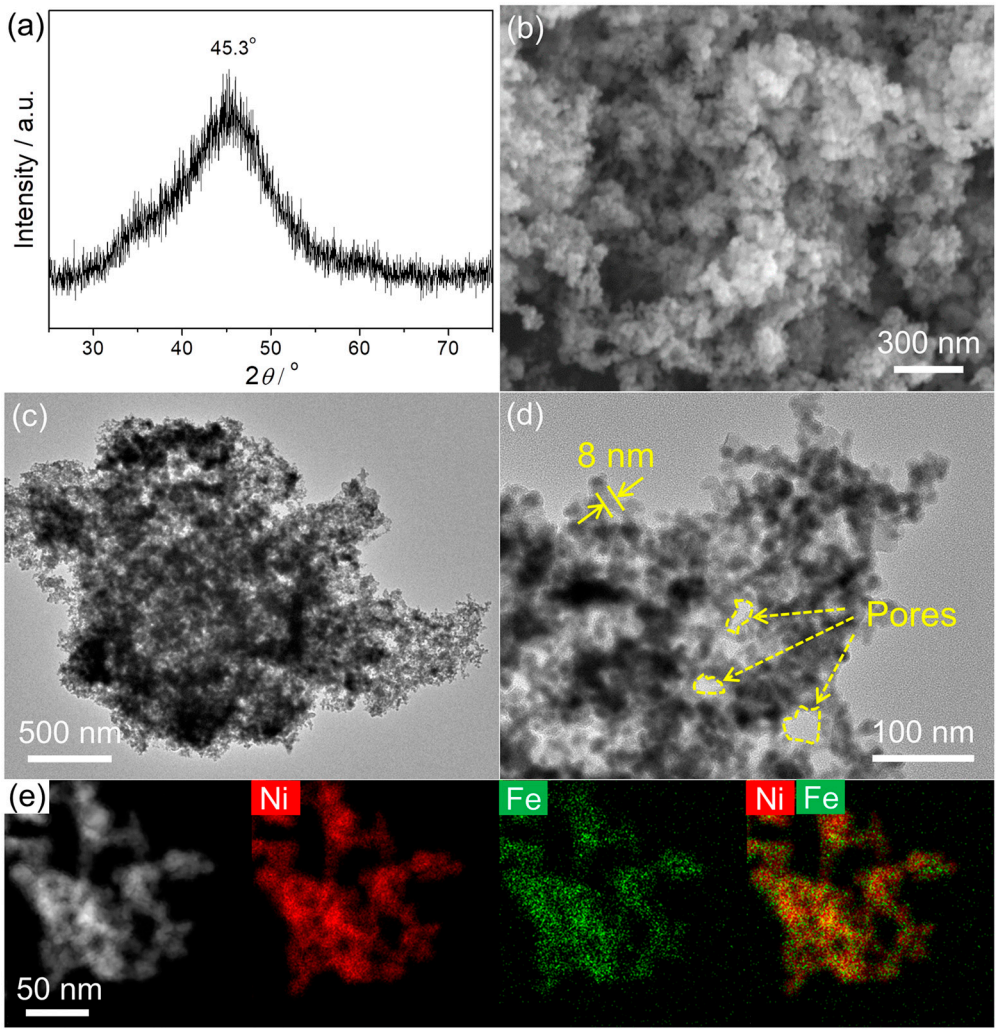

Figure 2. (**a**) XRD pattern, (**b**) SEM image, (**c**) TEM image, (**d**) HRTEM image (the arrows p pores), (**e**) HAADF-STEM and elemental mapping images of the NiFe-21 nanoaggregates.

The chemical composition and valence states of the as-fabricated NiFe nanoaggregates were revealed by X-ray photoelectron spectroscopy (XPS) measurements, especially the oxygen vacancies, which were essential for analyzing the electrocatalytic properties of these nanocatalysts. The full XPS spectra of the three NiFe nanoaggregates are shown in Figure S5. The elemental Ni and Fe can be clearly observed, and the presence of O was due

to the partial oxidation of the nanomaterials in air. The relative atomic contents of Ni and Fe in the three NiFe nanoaggregates obtained from the XPS results are displayed in Table S1. The proportion of Ni atoms in the catalysts gradually increased with the increasing Ni/Fe values of the precursors, and the molar ratio values of Ni/Fe are consistent with the EDX results. In order to further investigate the composition of each elemental valence state in the three nanomaterials, the respective XPS spectra of Ni, Fe, and O were analyzed. Figure 3a shows the high-resolution Ni 2p XPS spectrum of the NiFe-21 nanoaggregates. The peaks located at 852.8, 855.9, 858.2, and 861.6 eV represent Ni^0, Ni^{2+}, Ni^{3+}, and satellite peaks, respectively. In comparison with high-resolution Ni 2p XPS spectrum of NiFe-11 and NiFe-31 (Figure 3b,c), the amount of metallic Ni in NiFe-21 was the highest, which promoted the electron transport and thereby boosted the OER kinetics to being the fastest. This may have arisen from the doping of Fe, which can effectively prevent further oxidation of Ni and regulate the chemical states of Ni species by chemical tailoring because Fe is easier to oxidize with respect to Ni [39]. The high-resolution Fe 2p XPS spectrum of the NiFe-21 nanoaggregates is shown in Figure 3d. The peaks located at 706.6 eV and 712.2 eV correspond to Fe^0 and $Fe^{2+/3+}$, respectively. After calculation, the value of $Fe^0/Fe^{2+/3+}$ in NiFe-21 was determined to be 0.43, smaller than that of NiFe-11 (0.65, Figure 3e) and NiFe-31 (1.90, Figure 3f), implying the Fe mainly existed in the oxidized state.

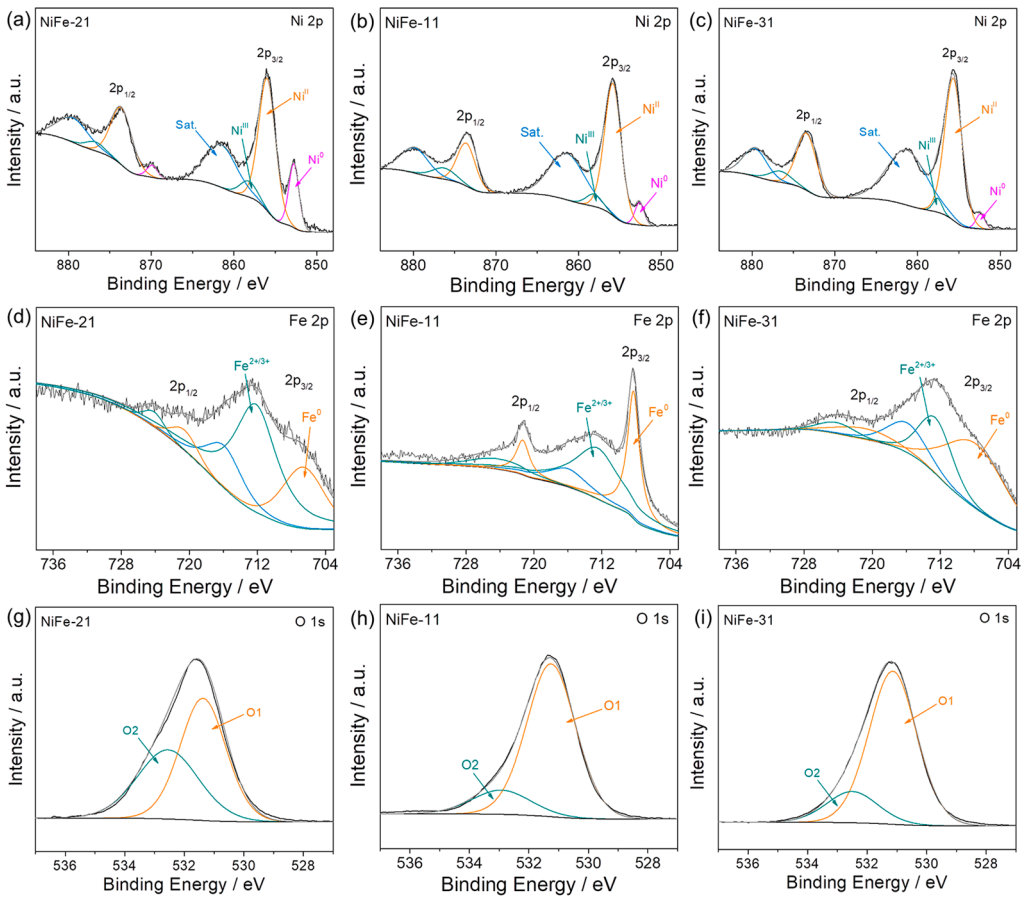

Figure 3. (**a**–**c**) High-resolution Ni 2p XPS spectra, (**d**–**f**) Fe 2p XPS spectra, and (**g**–**i**) O 1s XPS spectra of NiFe-21, NiFe-11, and NiFe-31, respectively.

In addition, the electronic states of O in these three NiFe nanomaterials were also investigated and are displayed in Figure 3g–i. The high-resolution O 1s XPS spectrum of NiFe-21 nanoaggregates, shown in Figure 3g, convolved into two characteristic peaks located at 531.1 eV and 532.2 eV, which correspond to the metal-bound oxygen atoms (O1) and the low-coordination defective oxygen (O2), respectively [40]. The value of O2/O1

in NiFe-21 was also the highest compared to that of NiFe-11 and NiFe-31, suggesting the most abundant oxygen vacancies were in the NiFe-21 nanoaggregates. Abundant oxygen vacancies are beneficial to the adsorption of water molecules, which eventually leads to the improvement of OER activity. According to the above analysis, the feeding molar ratio of Fe was important to modifying the electronic structure of Ni in the as-synthesized NiFe nanoaggregates and enhancing the OER performance.

To evaluate the electrocatalytic activities of as-synthesized NiFe samples, the electrochemically active surface area (ECSA) measured by double-layer capacitance (C_{dl}) was greatly important. Based on the CV plots, the C_{dl} of the NiFe-21 nanoaggregates was 0.37 mF cm^{-2} (Figure S6a,b), which is higher than that of NiFe-11 (0.19 mF cm^{-2}, Figure S6c,d) and NiFe-31 (0.24 mF cm^{-2}, Figure S6e,f). The higher C_{dl} value of the NiFe-21 nanoaggregates suggests a larger catalytically relevant surface area, implying superior electrochemical performance. This may have been due to the collapse of the 3D interconnected structure when the Fe content was low, resulting in a decrease in active sites, whereas the higher Fe content may have led to a reduction in real active sites on the Ni species, thus leading to poor activity. The OER performance of the NiFe-21 nanoaggregates and other contrast samples was initially evaluated by linear sweep voltammetry (LSV) tests in O_2-saturated 1 M KOH solution. Figure 4a shows the typical OER polarization curves of the three as-synthesized NiFe nanocatalysts and commercial RuO_2 catalysts. Obviously, only the NiFe-21 catalyst had an anodic peak from 1.3 to 1.5 V (vs. RHE), compared with the NiFe-11, NiFe-31, and RuO_2 catalysts, which was due to the oxidation of Ni. The combined action of Ni and NiO may have resulted in the H−O bond being easier to dissociate and the active species oxidizing more lightly on the NiFe-21 nanoaggregates under the same conditions, thereby promoting OER activity. The potential at the current density of 10 mA cm^{-2} is a significant experimental parameter for OER. As summarized in Figure 4b, the NiFe-21 nanoaggregates displayed the lowest overpotential of 0.35 V in comparison with that of NiFe-11 (0.40 V), NiFe-31 (0.39 V), and RuO_2 (0.36 V) at the current density of 10 mA cm^{-2}, as well as other reported catalysts (Table S2). What is more, the NiFe-21 nanoaggregates showed a higher current density than that of other compared catalysts at a potential of 1.65 V (vs. RHE), indicating superior activity of the NiFe-21 nanoaggregates towards OER. The corresponding Tafel slope is the most essential parameter for estimating the reaction kinetics [8,41].

As shown in Figure 4c, the Tafel slope of NiFe-21 nanoaggregates was 76.9 mV dec^{-1}, which is smaller than the 84.6 mV dec^{-1} at NiFe-11, 85.2 mV dec^{-1} at NiFe-31, and 80.1 mV dec^{-1} at RuO_2. The NiFe-21 nanoaggregates had the lowest Tafel slope, meaning that they provided the highest kinetic current density at the same applied potential, indicating outstanding intrinsic OER kinetics. The superior OER activity of NiFe-21 compared with NiFe-11 and NiFe-31 can be explained by the doped amounts of Fe. The incorporation of Fe adjusted the electronic structures of Ni, which created more oxygen vacancies and decreased the energy barrier of water adsorption, thereby promoting the formation of active intermediates and accelerating the oxygen generation. If the Ni content is high, the interconnected 3D structure would collapse because the excessive Ni atoms would be reduced alone, leading to a decrease in active sites and less oxygen vacancies due to the low Fe content, thus poor OER activity. Although the oxygen vacancies increased in the case of the higher Fe amounts, the real active sites on the Ni species decreased when the amount of Fe was continually increasing, leading to the degradation of the OER activity.

The long-term stability is another crucial parameter for catalysts when evaluating OER performance in practical applications. For the accelerated durability tests (ADTs), the OER polarization curves of the three NiFe catalysts and commercial RuO_2 catalysts before and after 5000 potential cycles are displayed in Figure S7a. Clearly, the NiFe-21 nanoaggregates showed an overpotential of 0.36 V at a current density of 10 mA cm^{-2}, which is only 0.01 V positive shift after ADTs (Figure S7b), whereas the overpotential of other compared catalysts increase to 0.42 V (NiFe-11), 0.44 V (NiFe-31), and 0.42 V (RuO_2). Similarly, at the potential of 1.65 V (vs. RHE), the current density of NiFe-21 nanoaggregates deceased from

24.8 mA cm^{-2} to 19.9 mA cm^{-2} after 5000 cycles (Figure S7c), which is lower than that of other reference catalysts. In addition, a chronoamperometry test (CA) was also carried out to study the durability of NiFe-21 nanoaggregates. As displayed in Figure 4d, the *i-t* curve of the as-prepared NiFe-21 nanoaggregates showed a higher current density and a slower current decay than that of the commercial RuO_2 catalysts during the tests. After 20,000 s, the NiFe-21 nanoaggregates maintained 86.3% of the initial current density, whereas the commercial RuO_2 maintained only 69.3%. These measurement results indicate that the as-synthesized NiFe-21 nanoaggregates had the best stability for OER compared to the reference samples.

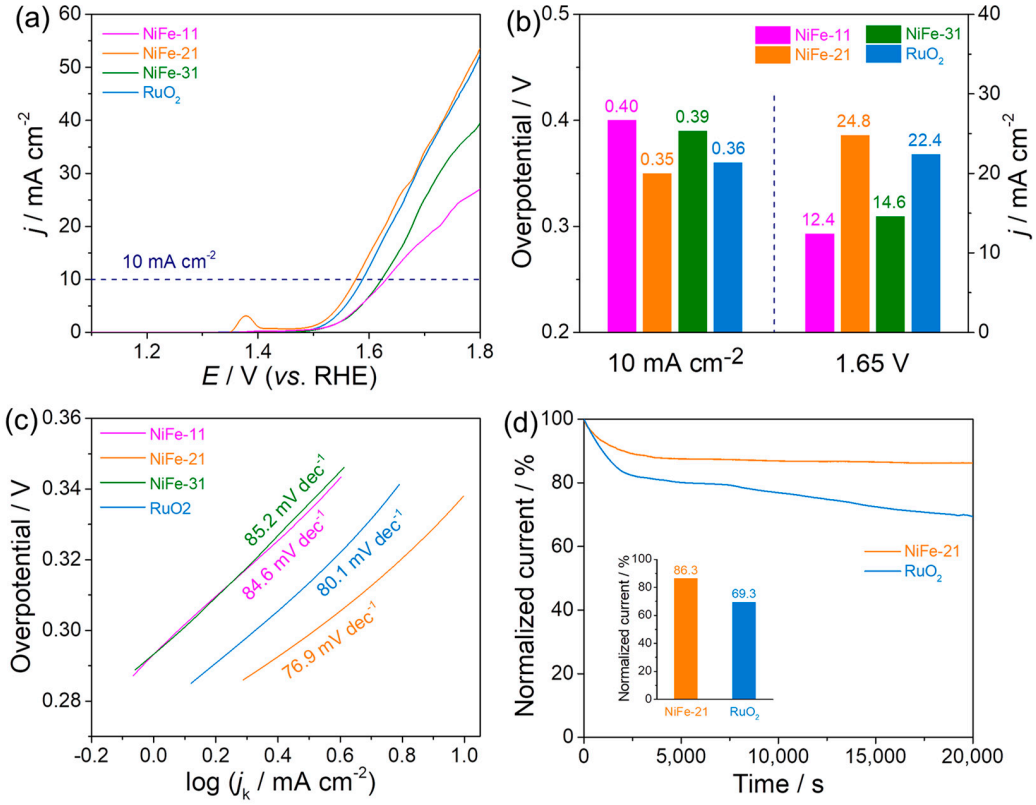

Figure 4. (**a**) OER polarization curves of NiFe-11, NiFe-21, NiFe-31, and commercial RuO_2 catalysts recorded in O_2-saturated 1 M KOH solution at a scan rate of 5 mV s^{-1} and a rotation rate of 1600 rpm. (**b**) Comparison of the overpotential at a current density of 10 mA cm^{-2} and the current density at a potential of 1.65 V. (**c**) Corresponding Tafel slopes. (**d**) CA tests of the NiFe-21 and RuO_2 catalysts in O_2-saturated 1 M KOH solution.

The superior OER activity and stability of the amorphous NiFe nanoaggregates can be ascribed to the porous 3D structure and the incorporation of Fe components. Specifically, (i) the 3D structure composed of interconnected small nanograins had abundant accessible active sites and large surface area, which can enhance the electrocatalytic activity of OER; (ii) the intrinsic 3D backbone structure of the cyanogel not only facilitated the electron transfer along the backbones but also decreased agglomeration and deactivation of NiFe nanoaggregates, which is beneficial to improving the durability for OER; (iii) the high porosity promoted mass diffusion and transport during the electrocatalytic process, which promoted the reaction kinetics of OER; and (iv) the adjustment of the Ni electronic structure and the enriched oxygen vacancies arising from the incorporation of Fe increased the efficient adsorption of $-OH/H_2O$, thus promoting the OER performance.

3. Experimental Section

3.1. Materials and Chemicals

Nickel chloride ($NiCl_2$), sodium hexacyanoferrate (II) ($Na_4Fe(CN)_6$), and sodium borohydride ($NaBH_4$) were purchased from Sinopharm Chemical Reagent Co., Ltd. (Shanghai, China). Commercial RuO_2 was obtained from Johnson Matthey Corporation (Shanghai, China). All chemicals and reagents were used without further purification. All of the aqueous solutions were prepared using Millipore water with a resistivity of 18.2 MΩ (Zhenjiang, China).

3.2. Synthesis of Amorphous NiFe-21 Nanoaggregates

In a typical synthesis, 2 mL of 0.5 M $NiCl_2$ and 1 mL of 0.5 M $Na_4Fe(CN)_6$ aqueous solutions were initially mixed at room temperature to form Ni-Fe cyanogels after standing for two hours. Then, 6 mL of 6 M freshly prepared $NaBH_4$ solution were added to the Ni-Fe cyanogels slowly, and the resulting mixture stood for an additional 36 h. After the reaction, the black NiFe nanoaggregates were separated by centrifugation at 12,000 rpm for 4 min, washed several times with water and ethanol, and then dried at 40 °C for 12 h in a vacuum oven.

3.3. Synthesis of Other Samples NiFe-11 and NiFe-31

In a typical synthesis, 2 mL of 0.5 M $NiCl_2$ and 2 mL of 0.5 M $Na_4Fe(CN)_6$ aqueous solutions were initially mixed at room temperature to form Ni-Fe cyanogels after standing for two hours. Then, 6 mL of 6 M freshly prepared $NaBH_4$ solution were added to the Ni-Fe cyanogels slowly, and the resulting mixture stood for an additional 36 h. After the reaction, the black NiFe-11 was separated by centrifugation at 12,000 rpm for 4 min, washed several times with water and ethanol, and then dried at 40 °C for 12 h in a vacuum oven. The NiFe-31 was obtained with 3 mL of 0.5 M $NiCl_2$ and 1 mL of 0.5 M $Na_4Fe(CN)_6$ aqueous solutions under the same experimental conditions.

3.4. Physical Characterization

The morphology and structure of the products were measured with Hitachi S-4800 scanning electron microscopy (SEM) and JEOL JEM-2010 transmission electron microscopy (TEM). High-resolution TEM (HRTEM), energy-dispersive X-ray (EDX), high-angle annular dark field–scanning transmission electron microscopy (HAADF-STEM) and elemental mapping measurements were carried out on an FEI Tecnai G2 F20 microscope, which was built as an accessory on the JEOL JEM-2100F. The Fourier transform infrared (FT-IR) spectra were obtained with a Nicolet 520 SXFTIR spectrometer. The phase purity and crystallinity of the products were confirmed by X-ray diffraction (XRD) on a Model D/max-rC X-ray diffractometer using a Cu Kα radiation source (λ = 1.5406 Å) and operating at 40 kV and 100 mA. X-ray photoelectron spectroscopy (XPS) tests were performed on a Thermo VG Scientific ESCALAB 250 spectrometer with a monochromatic Al Kα X-ray source (1486.6 eV photons). The binding energy was trued with respect to C1s at 284.6 eV.

3.5. Electrochemical Measurements

All electrochemical experiments were performed on a CHI 760D electrochemical workstation (CH Instruments, Chenhua Co., Shanghai, China) at 25 °C. A standard three-electrode system was used for all electrochemical experiments, which was made up of a graphite rod as the auxiliary electrode, a saturated calomel reference electrode protected by a Luggin capillary with a KCl solution as the reference electrode, and a glassy carbon rotating disk electrode (RDE, 5 mm in diameter, 0.196 cm^{-2}) modified with catalysts as the working electrode. All potentials in this work were recorded with respect to a reversible hydrogen electrode (RHE) using the following equation: $E_{RHE} = E_{SCE} + 0.242\ V + 0.0591pH$. The catalyst suspension was prepared by dispersing 5 mg of catalyst in 1 mL of solution containing 0.9 mL of deionized water and 0.1 mL of 0.5 wt% Nafion solution followed by ultrasonication for 30 min. For the immobilization of the catalyst, 10 μL of the catalyst

suspension were dropped onto the electrode surface and then dried at ambient temperature. The mass loading of the catalyst on the prepared electrode was 0.255 mg cm^{-2}. CV was performed in an N_2-saturated 1 M KOH solution. The OER tests were carried out in O_2-saturated 1 M KOH solution with a sweep rate of 5 mV s^{-1} and a rotation rate of 1600 rpm. The ECSA of the catalyst was obtained by testing the double-layer capacitance (C_{dl}) method under 1 M KOH electrolyte test conditions. Meanwhile, the C_{dl} values were calculated using equations by virtue of CV curves with different scan rates. The ECSA has a certain positive relationship with the C_{dl}, and thus the catalysts could be evaluated in terms of the C_{dl} value to compare the number of active sites in the materials with the ECSA. The specific calculation equation is $i = \nu C_{dl}$, where i is the current density and ν is the scan rate. Similarly, the OER kinetic performance of the catalyst could be compared by the Tafel slope, calculated from the LSV curves of the catalysts. The specific calculation equation is $\eta = a + b\log|j|$, where η is the overpotential, b is the Tafel slope, and j is the current density.

4. Conclusions

To sum up, we successfully synthesized an amorphous NiFe nanoaggregate through a simple cyanogel-derived synthetic strategy with $NaBH_4$ as a reducing agent at room temperature. The as-synthesized amorphous NiFe nanoaggregates had a porous 3D structure composed of interconnected small nanograins, which resulted from the characteristic 3D backbone structure of the cyanogels hampering the migration of reduced metal nuclei and resulting in the growth of metals along the 3D skeletons. The incorporation of Fe modified the electronic structure of Ni and increased the number of oxygen vacancies, which were studied by adjusting the feeding molar ratio of Ni/Fe. Because of the porous 3D structure and plentiful oxygen vacancies, the amorphous NiFe-21 nanoaggregates had abundant accessible active sites and a large surface area, exhibiting superior activity and stability for OER in comparison with the reference NiFe-11 and NiFe-31 catalysts prepared with different feeding molar ratios and even superior activity and stability compared to commercial RuO_2 catalysts. This work provides a simple strategy to develop highly efficient OER electrocatalysts with excellent activity and stability by using earth-abundant and cost-effective 3*d*-transition metal elements, which would accelerate the manufacture of advanced electrocatalysts for water splitting in the future.

Supplementary Materials: The following supporting information can be downloaded at: https://www.mdpi.com/article/10.3390/catal13091261/s1. Equation S1 Formation equation of cyanogel from transition metal cyanometalates and tetrachlorometalates in aqueous solution. Equation S2 Equation of chemical reaction between cyanogel and $NaBH_4$. Figure S1 FT-IR spectra of (a) the $NiCl_2/Na_4Fe(CN)_6$ cyanogel and (b) pure $Na_4Fe(CN)_6$. Figure S2 SEM images of (a-b) the NiFe-11 catalysts and (c-d) the NiFe-31 catalysts. Figure S3 (a) STEM image and (b) EDX line scanning profile of the NiFe nanoaggregates. Figure S4 EDX spectrum of the NiFe-21 nanoaggregates. Figure S5 XPS survey scan spectra of the NiFe catalysts with different Ni/Fe molar ratio. Figure S6 (a), (c) and (e) CV curves of NiFe-21, NiFe-11, NiFe-31 at different scan rates in 1 M KOH. (b), (d) and (f) Plots of the capacitive current density at 1.23 V against the scan rate of the NiFe-21, NiFe-11, NiFe-31. Figure S7 (a) OER polarization curves before and after 5000 cycles of the NiFe-21, NiFe-11, NiFe-31 and commercial RuO_2 catalysts. (b) Comparison of the overpotentials at the current density of 10 mA cm^{-2} before and after 5000 cycles. (c) Comparison of the current density at the potential of 1.65 V before and after 5000 cycles. Table S1 The atomic contents of Ni and Fe in the NiFe-11, NiFe-21 and NiFe-31 nanocatalysts obtained from the full XPS results. Table S2 Comparison of the OER activity of the amorphous NiFe-21 nanoaggregates in 1 M KOH electrolyte with other electrocatalysts previously reported [42–50].

Author Contributions: Conceptualization, Z.L. and J.Y.; methodology, S.L., J.W. and M.Z.; formal analysis, Z.L., W.S. and X.Z.; writing—original draft preparation, S.L. and J.W.; writing—review and editing, Z.L. and P.R. All authors have read and agreed to the published version of the manuscript.

Funding: This research was funded by the Natural Science Foundation of Jiangsu Province (BK20201004).

Data Availability Statement: Data are contained within the article.

Conflicts of Interest: The authors declare no conflict of interest.

References

1. Hu, E.; Feng, Y.F.; Nai, J.W.; Zhao, D.; Hu, Y.; Lou, X.W.D. Construction of hierarchical Ni-Co-P hollow nanobricks with oriented nanosheets for efficient overall water splitting. *Energy Environ. Sci.* **2018**, *11*, 872–880. [CrossRef]
2. Guan, D.Q.; Xu, H.Y.; Zhang, Q.W.; Huang, Y.C.; Shi, C.L.; Chang, Y.C.; Xu, X.M.; Tang, J.Y.; Gu, Y.X.; Pao, C.W.; et al. Identifying A Universal Activity Descriptor and a Unifying Mechanism Concept on Perovskite Oxides for Green Hydrogen Production. *Adv. Mater.* **2023**, 2305074. [CrossRef] [PubMed]
3. Li, W.Q.; Zhang, H.; Zhang, K.; Cheng, Z.Z.; Chen, H.P.; Tan, G.; Feng, X.; Wang, L.Y.; Mu, S.C. Altered electronic structure of trimetallic FeNiCo-MOF nanosheets for efficient oxygen evolution. *Chem. Commun.* **2023**, *59*, 4750–4753. [CrossRef]
4. Qiu, Z.; Ma, Y.; Edvinsson, T. In operando Raman investigation of Fe doping influence on catalytic NiO intermediates for enhanced overall water splitting. *Nano Energy* **2019**, *66*, 104118. [CrossRef]
5. Xu, X.M.; Pan, Y.L.; Ge, L.; Chen, Y.B.; Mao, X.; Guan, D.Q.; Li, M.R.; Zhong, Y.J.; Hu, Z.W.; Peterson, V.K.; et al. High-Performance Perovskite Composite Electrocatalysts Enabled by Controllable Interface Engineering. *Small* **2021**, *17*, 2101573. [CrossRef] [PubMed]
6. Bernicke, M.; Ortel, E.; Reier, T.; Bergmann, A.; Ferreira de Araujo, J.; Strasser, P.; Kraehnert, R. Iridium Oxide Coatings with Templated Porosity as Highly Active Oxygen Evolution Catalysts: Structure-Activity Relationships. *ChemSusChem* **2015**, *8*, 1908–1915. [CrossRef]
7. Zhang, L.J.; Jang, H.; Liu, H.H.; Kim, M.G.; Yang, D.J.; Liu, S.G.; Liu, X.; Cho, J. Sodium-Decorated Amorphous/Crystalline RuO_2 with Rich Oxygen Vacancies: A Robust pH-Universal Oxygen Evolution Electrocatalyst. *Angew. Chem. Int. Ed.* **2021**, *60*, 18821–18829. [CrossRef]
8. Liu, Z.Y.; Li, J.H.; Zhang, J.; Qin, M.H.; Yang, G.X.; Tang, Y.W. Ultrafine Ir Nanowires with Microporous Channels and Superior Electrocatalytic Activity for Oxygen Evolution Reaction. *ChemCatChem* **2020**, *12*, 3060–3067. [CrossRef]
9. Sakamaki, A.; Yoshida-Hirahara, M.; Kurokawa, H.; Ogihara, H. One-Step Synthesis of Highly Active NiFe Electrocatalysts for the Oxygen Evolution Reaction. *Langmuir* **2022**, *38*, 5525–5531. [CrossRef]
10. Tan, S.F.; Ouyang, W.M.; Ji, Y.J.; Hong, Q.W. Carbon wrapped bimetallic NiCo nanospheres toward excellent HER and OER performance. *J. Alloys Compd.* **2021**, *889*, 161528. [CrossRef]
11. Liu, Z.Y.; Wan, J.X.; Li, M.; Shi, Z.P.; Liu, J.H.; Tang, Y.W. Synthesis of Co/CeO_2 hetero-particles with abundant oxygen-vacancies supported by carbon aerogels for ORR and OER. *Nanoscale* **2022**, *14*, 1997–2003. [CrossRef]
12. Zeng, X.J.; Zhang, Q.Q.; Shen, Z.Y.; Zhang, H.Q.; Wang, T.; Liu, Z.Y. Doping and Vacancy Engineering in a Sandwich-like g-C_3N_4/$NiCo_2O_4$ Heterostructure for Robust Oxygen Evolution. *ChemNanoMat* **2022**, *8*, e202200191. [CrossRef]
13. Krishnamurthy, P.; Maiyalagan, T.; Panomsuwan, G.; Jiang, Z.Q.; Rahaman, M. Iron-Doped Nickel Hydroxide Nanosheets as Efficient Electrocatalysts in Electrochemical Water Splitting. *Catalysts* **2023**, *13*, 1095. [CrossRef]
14. Anantharaj, S.; Karthik, P.E.; Kundu, S. Petal-like hierarchical array of ultrathin $Ni(OH)_2$ nanosheets decorated with $Ni(OH)_2$ nanoburls: A highly efficient OER electrocatalyst. *Catal. Sci. Technol.* **2017**, *7*, 882–893. [CrossRef]
15. Lei, X.; Qing, J.C.; Weng, L.T.; Li, S.M.; Peng, R.Z.; Wang, W.; Wang, J.L. Porous FeP/CoP heterogeneous materials as efficient alkaline oxygen evolution reaction (OER) catalysts. *New J. Chem.* **2022**, *46*, 15351–15357. [CrossRef]
16. Li, S.M.; Bai, L.; Shi, H.B.; Hao, X.F.; Chen, L.; Qin, X.J.; Shao, G.J. Mo-doped CoP nanosheets as high-performance electrocatalyst for HER and OER. *Ionics* **2021**, *27*, 3109–3118. [CrossRef]
17. Han, M.N.; Shi, M.J.; Wang, J.; Zhang, M.L.; Yan, C.; Jiang, J.T.; Guo, S.H.; Sun, Z.Y.; Guo, Z.H. Efficient bifunctional Co/N dual-doped carbon electrocatalysts for oxygen reduction and evolution reaction. *Carbon* **2019**, *153*, 575–584. [CrossRef]
18. Guo, D.Y.; Zeng, Z.H.; Wan, Z.X.; Li, Y.; Xi, B.; Wang, C.X. A CoN-based OER Electrocatalyst Capable in Neutral Medium: Atomic Layer Deposition as Rational Strategy for Fabrication. *Adv. Funct. Mater.* **2021**, *31*, 2101324. [CrossRef]
19. Pei, Z.H.; Lu, X.F.; Zhang, H.B.; Li, Y.X.; Luan, D.Y.; Lou, X.W. Highly Efficient Electrocatalytic Oxygen Evolution over Atomically Dispersed Synergistic Ni/Co Dual Sites. *Angew. Chem. Int. Ed.* **2022**, *61*, e202207537. [CrossRef]
20. Peng, L.S.; Yang, N.; Yang, Y.Q.; Wang, Q.; Xie, X.Y.; Sun-Waterhouse, D.X.; Shang, L.; Zhang, T.R.; Waterhouse, G.I.N. Atomic Cation-Vacancy Engineering of NiFe-Layered Double Hydroxides for Improved Activity and Stability towards the Oxygen Evolution Reaction. *Angew. Chem. Int. Ed.* **2021**, *60*, 24612–24619. [CrossRef]
21. Wang, Y.Y.; Qiao, M.; Li, Y.; Wang, S.Y. Tuning Surface Electronic Configuration of NiFe LDHs Nanosheets by Introducing Cation Vacancies (Fe or Ni) as Highly Efficient Electrocatalysts for Oxygen Evolution Reaction. *Small* **2018**, *14*, 1800136. [CrossRef]
22. Zhang, L.L.; Yang, Y.Q.; Zhu, H.Z.; Cheng, H.M.; Liu, G. Iron-doped NiS_2 microcrystals with exposed {001} facets for electrocatalytic water oxidation. *J. Colloid Interf. Sci.* **2022**, *608*, 599–604. [CrossRef] [PubMed]
23. Wan, J.X.; Liu, Z.Y.; Yang, X.Y.; Cheng, P.; Yan, C. Cyanogel-Derived Synthesis of Porous PdFe Nanohydrangeas as Electrocatalysts for Oxygen Reduction Reaction. *Nanomaterials* **2021**, *11*, 3382. [CrossRef] [PubMed]

24. Wang, Z.J.; Jin, M.X.; Zhang, L.; Wang, A.J.; Feng, J.J. Amorphous 3D pomegranate-like NiCoFe nanoassemblies derived by bi-component cyanogel reduction for outstanding oxygen evolution reaction. *J. Energy Chem.* **2021**, *53*, 260–267. [CrossRef]
25. Yan, H.J.; Xie, Y.; Wu, A.P.; Cai, Z.C.; Wang, L.; Tian, C.G.; Zhang, X.M.; Fu, H.G. Anion-Modulated HER and OER Activities of 3D Ni-V-Based Interstitial Compound Heterojunctions for High-Efficiency and Stable Overall Water Splitting. *Adv. Mater.* **2019**, *31*, e1901174. [CrossRef]
26. Zhou, Y.; Zeng, H.C. 3D Networks of CoFePi with Hierarchical Porosity for Effective OER Electrocatalysis. *Small* **2018**, *14*, 1704403. [CrossRef] [PubMed]
27. Chang, K.; Tran, D.T.; Wang, J.Q.; Kim, N.H.; Lee, J.H. A 3D hierarchical network derived from 2D Fe-doped NiSe nanosheets/carbon nanotubes with enhanced OER performance for overall water splitting. *J. Mater. Chem. A* **2022**, *10*, 3102–3111. [CrossRef]
28. Chauhan, M.; Reddy, K.P.; Gopinath, C.S.; Deka, S. Copper Cobalt Sulfide Nanosheets Realizing a Promising Electrocatalytic Oxygen Evolution Reaction. *ACS Catal.* **2017**, *7*, 5871–5879. [CrossRef]
29. Zha, Q.Q.; Xu, W.Y.; Li, X.L.; Ni, Y.H. Chlorine-doped alpha-Co(OH)$_2$ hollow nano-dodecahedrons prepared by a ZIF-67 self-sacrificing template route and enhanced OER catalytic activity. *Dalton T.* **2019**, *48*, 12127–12136. [CrossRef] [PubMed]
30. Wang, Y.; Sun, L.Z.; Lu, L.G.; Xu, D.D.; Hao, Q.L.; Liu, B. A sequential template strategy toward hierarchical hetero-metal phosphide hollow nanoboxes for electrocatalytic oxygen evolution. *J. Mater. Chem. A* **2021**, *9*, 3482–3491. [CrossRef]
31. Jiang, W.; Li, H.G.; Chen, Y.L.; Wu, Y.; Li, J.J.; Wang, X.; Huang, X.Q.; Lao, Y.X. OER properties of Ni-Co-CeO$_2$/Ni composite electrode prepared by magnetically induced jet electrodeposition. *Int. J. Hydrogen Energy* **2023**, *48*, 4287–4299. [CrossRef]
32. Goujani, M.J.; Alizadeh, M. One-step electrodeposition of Co-Fe electrocatalysts with micro/nano-cauliflower like structure for highly efficient oxygen evolution reaction (OER). *J. Alloys Compd.* **2023**, *960*, 170557. [CrossRef]
33. Heibel, M.; Kumar, G.; Wyse, C.; Bukovec, P.; Bocarsly, A.B. Use of sol-gel chemistry for the preparation of cyanogels as ceramic and alloy precursors. *Chem. Mater.* **1996**, *8*, 1504–1511. [CrossRef]
34. Vondrova, M.; McQueen, T.M.; Burgess, C.M.; Ho, D.M.; Bocarsly, A.B. Autoreduction of Pd−Co and Pt−Co cyanogels: Exploration of cyanometalate coordination chemistry at elevated temperatures. *J. Am. Chem. Soc.* **2008**, *130*, 5563–5572. [CrossRef] [PubMed]
35. Zhang, L.; Wan, L.; Ma, Y.R.; Chen, Y.; Zhou, Y.M.; Tang, Y.W.; Lu, T.H. Crystalline palladium–cobalt alloy nanoassemblies with enhanced activity and stability for the formic acid oxidation reaction. *Appl. Catal. B-Environ.* **2013**, *138*, 229–235. [CrossRef]
36. Zhang, L.; Lu, D.K.; Chen, Y.; Tang, Y.W.; Lu, T.H. Facile synthesis of Pd–Co–P ternary alloy network nanostructures and their enhanced electrocatalytic activity towards hydrazine oxidation. *J. Mater. Chem. A* **2014**, *2*, 1252–1256. [CrossRef]
37. Liu, Z.Y.; Fu, G.T.; Li, J.H.; Liu, Z.Q.; Xu, L.; Sun, D.M.; Tang, Y.W. Facile synthesis based on novel carbon-supported cyanogel of structurally ordered Pd_3Fe/C as electrocatalyst for formic acid oxidation. *Nano Res.* **2018**, *11*, 4686–4696. [CrossRef]
38. Zhang, G.J.; Zhang, L.; Shen, L.P.; Chen, Y.; Zhou, Y.M.; Tang, Y.W.; Lu, T.H. Synthesis and Electrocatalytic Properties of Palladium Network Nanostructures. *ChemPlusChem* **2012**, *77*, 936–940. [CrossRef]
39. Guo, P.; Wang, Z.J.; Zhang, T.; Chen, C.; Chen, Y.L.; Li, H.J.; Hua, M.L.; Wei, S.X.; Lu, X.Q. Initiating an efficient electrocatalyst for water splitting via valence configuration of cobalt-iron oxide. *Appl. Catal. B-Environ.* **2019**, *258*, 117968. [CrossRef]
40. Xu, H.; Shi, Z.X.; Tong, Y.X.; Li, G.R. Porous Microrod Arrays Constructed by Carbon-Confined NiCo@$NiCoO_2$ Core@Shell Nanoparticles as Efficient Electrocatalysts for Oxygen Evolution. *Adv. Mater.* **2018**, *30*, 1705442. [CrossRef]
41. Zhuang, L.Z.; Ge, L.; Yang, Y.S.; Li, M.R.; Jia, Y.; Yao, X.D.; Zhu, Z.H. Ultrathin Iron-Cobalt Oxide Nanosheets with Abundant Oxygen Vacancies for the Oxygen Evolution Reaction. *Adv. Mater.* **2017**, *29*, 1606793. [CrossRef] [PubMed]
42. Liang, H.F.; Meng, F.; Caban-Acevedo, M.; Li, L.S.; Forticaux, A.; Xiu, L.C.; Wang, Z.C.; Jin, S. Hydrothermal Continuous Flow Synthesis and Exfoliation of NiCo Layered Double Hydroxide Nanosheets for Enhanced Oxygen Evolution Catalysis. *Nano Lett.* **2015**, *15*, 1421–1427. [CrossRef]
43. Gao, M.R.; Sheng, W.C.; Zhuang, Z.B.; Fang, Q.R.; Gu, S.; Jiang, J.; Yan, Y.S. Efficient Water Oxidation Using Nanostructured α-Nickel-Hydroxide as an Electrocatalyst. *J. Am.Chem. Soc.* **2014**, *136*, 7077–7084. [CrossRef] [PubMed]
44. Shuai, C.; Mo, Z.L.; Niu, X.H.; Yang, X.; Liu, G.G.; Wang, J.; Liu, N.J.; Guo, R.B. Hierarchical $NiCo_2S_4$ nanosheets grown on grapheme to catalyze the oxygen evolution reaction. *J. Mater. Sci.* **2019**, *55*, 1627–1636. [CrossRef]
45. Song, F.; Hu, X.L. Exfoliation of layered double hydroxides for enhanced oxygen evolution catalysis. *Nat. Commun.* **2014**, *5*, 4477. [CrossRef]
46. Cheng, H.; Su, Y.Z.; Kuang, P.Y.; Chen, G.F.; Liu, Z.Q. Hierarchical $NiCo_2O_4$ nanosheet-decorated carbon nanotubes towards highly efficient electrocatalyst for water oxidation. *J. Mater. Chem. A* **2015**, *3*, 19314–19321. [CrossRef]
47. Li, Y.G.; Hasin, P.; Wu, Y.Y. Ni_xCo_3-xO_4 Nanowire Arrays for Electrocatalytic Oxygen Evolution. *Adv. Mater.* **2010**, *22*, 1926–1929. [CrossRef]
48. Wang, J.; Li, K.; Zhong, H.X.; Xu, D.; Wang, Z.L.; Jiang, Z.; Wu, Z.J.; Zhang, X.B. Synergistic Effect between Metal-Nitrogen-Carbon Sheets and NiO Nanoparticles for Enhanced Electrochemical Water-Oxidation Performance. *Angew. Chem. Int. Ed.* **2015**, *54*, 10530–10534. [CrossRef]

49. Meng, L.X.; Xuan, H.C.; Wang, J.; Liang, X.H.; Li, Y.P.; Yang, J.; Han, P.D. Flower-like Co_3O_4@NiFe-LDH nanosheets enable high-performance bifunctionality towards both electrocatalytic HER and OER in alkaline solution. *J. Alloys Compd.* **2022**, *919*, 165877. [CrossRef]
50. Berger, M.; Popa, I.M.; Negahdar, L.; Palkovits, S.; Kaufmann, B.; Pilaski, M.; Hoster, H.; Palkovits, R. Elucidating the Influence of Intercalated Anions in NiFe LDH on the Electrocatalytic Behavior of OER: A Kinetic Study. *ChemElectroChem* **2023**, e202300235. [CrossRef]